A Mathematical Model for the Multiphase Transport and Reaction Kinetics in a Ladle with Bottom Powder Injection

WENTAO LOU and MIAOYONG ZHU

A computation fluid dynamics-population balance model-simultaneous reaction model (CFD-PBM-SRM) coupled model has been proposed to study the multiphase flow behavior and refining reaction kinetics in a ladle with bottom powder injection, and some new and important phenomena and mechanisms are presented. For the multiphase flow behavior, the effects of bubbly plume flow, powder particle motion, particle-particle collision and growth, particle-bubble collision and adhesion, and powder particle removal into top slag are considered. For the reaction kinetics, the mechanisms of multicomponent simultaneous reactions, including Al, S, Si, Mn, Fe, and O, at the multi-interface, including top slag-liquid steel interface, air-liquid steel interface, powder droplet-liquid steel interface, and bubble-liquid steel interface, are presented, and the effect of sulfur solubility in the powder droplet on the desulfurization is also taken into account. Model validation is carried out using hot tests in a 2-t induction furnace with bottom powder injection. The result shows that the powder particles gradually disperse in the entire furnace; in the vicinity of the bottom slot plugs, the desulfurization product CaS is liquid phase, while in the upper region of the furnace, the desulfurization product CaS is solid phase. The predicted sulfur contents by the present model agree well with the measured data in the 2-t furnace with bottom powder injection.

DOI: 10.1007/s11663-017-1058-x

I. INTRODUCTION

WITH the increase of demands for low-sulfur and ultralow-sulfur steel, high efficiency of desulfurization has become one of the main objectives in the clean steel production process since sulfur in most steel products is detrimental. To produce low-sulfur and ultralow-sulfur steel, a combined flowsheet process, including hot metal pretreatment-basic oxygen furnace (BOF) steelmaking-ladle refining, has been commonly practiced as an effective method in many iron and steel enterprises. However, it is nearly inevitable that this flowsheet is too long, and the metallurgical efficiency is low. The main drawbacks are as follows

(1) In the hot metal pretreatment process, multiple times skimming slag are needed before and after desulfurization, which would produce larger iron loss and lower metal yield. Furthermore, the molten iron cleanliness is threatened by stirring blades or top lance refractory.
(2) In the BOF process, the sulfur content of liquid steel will again increase by 0.004 to 0.012 pct due to the resulfurization from oxidizing slag and steel scrap, which obviously weaken the role of hot metal pretreatment. Therefore, the ladle second desulfurization is necessary to produce low-sulfur and ultralow-sulfur steel.
(3) In the ladle second desulfurization process, the top slag desulfurization in the ladle furnace (LF) ladle and top powder injection desulfurization in Ruhrstahl Heraeus (RH) or ladle have been well implemented to reduce the final sulfur content of liquid steel. However, in the LF ladle, the desulfurization efficiency is low due to smaller reaction specific surface area and slower mass-transfer rate at the top slag-liquid steel interface, and the entire desulfurization process needs more than 40 minutes. For the powder injection desulfurization with top lance, the desulfurization rate is fast and the processing cycle become short. However, the liquid steel cleanliness is threatened by top lance refractory, the splash and secondary pollution of liquid steel are serious, and the stability and flexibility of the process are also relatively poor.

WENTAO LOU and MIAOYONG ZHU are with the School of Metallurgy, Northeastern University, Shenyang 110819, China. Contact email: louwt@smm.neu.edu.cn
Manuscript submitted March 2, 2017.
Article published online August 25, 2017.

Recently, Zhu and his co-workers developed a new technology of bottom powder injection for ladle refining,[1–4] and the fine desulfurization powders are injected into liquid steel through bottom slot plugs in the ladle, as shown in Figure 1. Compared with the traditional desulfurization process, the new technology has many advantages, such as better kinetic conditions, less serious splashing, and higher powder use and desulfurization rate. In addition, there is also no steel cleanliness risk caused by lance refractory. Therefore, this technology has broad application prospects and attracts more and more attention, and it is necessary to reveal clearly the multiphase transport and reaction kinetics in the process of bottom powder injection in the ladle to improve metallurgical efficiency and effectiveness.

As shown in Figure 2, in the process of bottom powder injection, the multiphase flow transport and chemical reactions in the ladle are complex and mainly involve bubbly plume flow, powder flow, particle-particle and particle-bubble collision, adhesion and removal, powder-liquid steel interfacial reaction, top slag-liquid steel interfacial reaction, *etc*. These phenomena will occur simultaneously and interact with each other, which directly determines desulfurization efficiency and effectiveness. So far, the related research is still in the blank stage, but from the perspective of the powder transfer and reaction, the top lance powder injection process has many similar phenomena, and many researchers have proposed mathematical models[5–10] to describe the desulfurization kinetics. Furthermore, Jonsson *et al*.[12] and Andersson *et al*.[11,13] proposed mathematical models incorporating the thermodynamic reactions into the computational fluid dynamics (CFD) model to predict the top slag-liquid steel desulfurization behavior in the gas-stirred ladle. This literature provides an important reference to the study on the bottom power injection process. Even so, it should be noted that these studies mainly focused on the powder particle-liquid steel interfacial reaction and top slag-liquid steel interfacial reaction, and there are still many important transport and reaction mechanisms that have not been considered yet. Their details are as follows

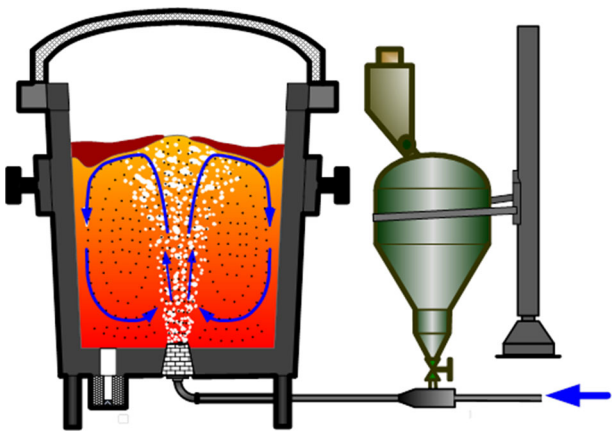

Fig. 1—Schematic diagram of the new technology of the ladle bottom powder injection.

(a) Powder particles adhered on bubbles. As shown in Figure 2, when the desulfurization powder particles are injected into the ladle accompanying gas blowing, part of them may be adhered on the bubble surface due to particle-bubble collisions in the bubbly plume zone, and then float following with the bubble, which in turn lowers the powder use and desulfurization rate. According to our recent publication,[14,15] the particle-bubble adhesion rate due to turbulence random collision, turbulent shear collision, and buoyancy collision is intense in the bubbly plume zone and plays an important role in the particle transport in the liquid steel. Therefore, the effect of powder particles adhered on bubbles on the desulfurization behavior should be taken into account in the bottom powder injection process.

(b) Powder particle growth due to collisions. The size of the powder particle has an important effect on the powder transport and desulfurization kinetic parameters, such as powder floating velocity, powder-bubble adhesion rate, powder-liquid steel contact area and reaction rate, *etc*. In the turbulent flow systems, the powder particles will gradually grow due to particle-particle turbulent shear collisions and stokes buoyancy collisions, which are mainly affected by the turbulent flow and particle concentration.[14] In the bottom powder injection process, a large number of powder particles are injected into liquid steel and mainly disperse in the bubbly plume zone with intense turbulent flow. Therefore, the effect of powder particle collision and growth on the desulfurization behavior should be taken into account.

(c) Powder particles removed into top slag. Theoretically, the longer the residence time of powder in liquid steel, the more convenient to improve the powder use and desulfurization efficiency. In the ladle, the fine particles can be removed into top slag due to their own floating motion or bubble-carrying motion, which, in turn, affect the powder residence time and desulfurization efficiency. Furthermore, the reaction product of powder desulfurization is also a kind of inclusion and may have a detrimental effect on the quality of steel, especially when coagulated large-size powder particles remain in steel products. Therefore, the effect of powder particle removal on the desulfurization efficiency and liquid steel cleanliness cannot be ignored.

(d) Multicomponent simultaneous reaction behavior. In the actual refining process, the mixtures of various powders or premelted slags, which include multiple oxide components, such as CaO, Al_2O_3, and SiO_2, are always added into hot metal or liquid steel for desulfurization due to their low melting point and high mass-transfer rate compared with the pure calcium oxide.[16–19] Therefore, the multiple reactions involving (CaO)-(Al_2O_3)-(SiO_2)-(FeO)-(MnO)-[S]-[O] would occur simultaneously at the powder-liquid steel interface, which determines the interfacial oxygen activity and affects significantly the desulfurization behavior. However, until now, most of the literature[5–10] only focused on the sulfur

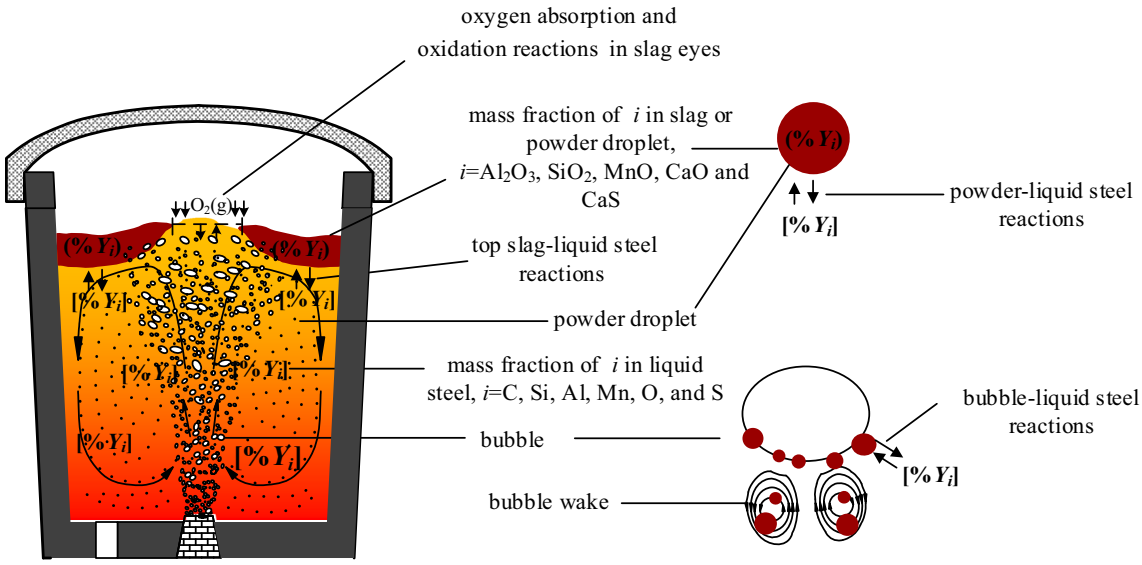

Fig. 2— Schematic diagram of the multiphase flow transport and reaction kinetics in the ladle bottom powder injection.

element reaction and ignored the effect of other elements. In our recent publications,[20,21] the mechanism of multicomponent simultaneous reaction was described in detail and validated for the top slag-liquid steel desulfurization behavior. These studies[20,21] showed that there was a dynamic balance between the multiple interfacial reactions involving dealumination, desilication, demanganization, and desulfurization, and the desulfurization efficiency was obviously influenced by other element reactions. Therefore, in the bottom powder injection process, the effect of multicomponent simultaneous reaction behavior on the desulfurization efficiency must be taken into account.

(e) Reaction between bubble and liquid steel. In the bubbly plume flow zone, a large amount of powder particles will be adhered to the bubble surface and become an integral part of the bubble. With the bubbles floating, these adsorbed particles will also contact and react with the molten steel, as shown in Figure 2, and their dynamic conditions are quite different from those of dispersion powders in liquid steel. Because the contact surface and time of bubble and liquid steel will obviously decrease more than that of dispersion particles and liquid steel. Additionally, in the bubbly plume zone, the adsorbed powder particles also appear to have random turbulent motion followed with bubbles, where the interphase mass-transfer rate will be different from that of dispersion powders in the liquid steel. Therefore, the reaction kinetics between bubble and liquid steel need to be considered separately.

(f) Effect of sulfur solubility in powder droplets. Many researchers have studied the physic-chemical behavior of sulfur in $CaO-Al_2O_3$ slag and pointed out that the solubility of CaS in the $CaO-Al_2O_3$ slag is about 4 mol pct and decreases with decreasing CaO content.[22–25] In the ladle, as the refining powder is injected into the liquid steel, the chemical reactions would strongly take place between the fine powder droplets and liquid steel, and the CaS concentration in droplets will rapidly increase, while CaO concentration will decrease. Once the sulfur reaches saturation, the solid phase of CaS will be produced, and the related thermodynamics and kinetics of desulfurization vary, which, in turn, affect the desulfurization efficiency. Therefore, the effect of sulfur solubility in powder droplets should be taken into account.

The objectives of this study are to present a mathematical model to describe the multiphase flow behavior and refining reaction kinetics in the ladle with bottom powder injection and try to predict the bubbly plume flow, powder particles flow and transport behavior, multicomponent reaction, and desulfurization efficiency more reasonably by considering the aforementioned important phenomena and mechanisms.

The present work is organized as follows. In Section II, a computation fluid dynamic-population balance model-simultaneous reaction model (CFD-PBM-SRM) couple model is constructed and described in detail. The CFD module is adopted to describe the multiphase turbulent flow behavior. The PBM module is adopted to describe the powder particle transport, size distribution, collision, and removal behavior. The SRM module is adopted to describe the refining reaction behavior involving $(CaO)-(Al_2O_3)-(SiO_2)-(FeO)-(MnO)-[S]-[O]$ multicomponent simultaneous reaction at different phase interfaces, namely, powder-liquid steel interface, bubble-liquid steel interface, top slag-liquid steel interface, and air-liquid steel interface. In Section III, the hot experiment of the bottom powder injection in the 2-t induction furnace is carried out, and the sulfur concentrations in liquid steel are detected with time. In Section IV, the mathematical model is verified and the comparisons between calculated and measured results are carried out to illustrate the practical performance of the present model, which will provide a theoretical basis

for further research investigating the desulfurization behavior under different kinetic conditions in the industrial ladle with bottom powder injection.

II. GOVERNING EQUATIONS FOR THE CFD-PBM-SRM COUPLED MODEL

A. *Assumptions*

The mathematical model for multiphase flow transport and reaction kinetics in the ladle is based on the following assumptions

(a) The liquid steel in the ladle is incompressible Newtonian fluid, and the turbulent flow is isotropic.
(b) The bubbles and powder particles are assumed to be spherical, and the diameter of bubbles is regarded as a constant during bubbles rising in the ladle.
(c) The refining powder particles in liquid steel are treated as droplets, because they include multiple oxide components and have low melting point.[16–19]
(d) Powder particle collision occurring between two spherical particles forms a larger spherical particle. Cluster formation due to collision between several particles is not considered.
(e) The particle reaching the top surface excluding slag eye is considered ideal absorption by the slag layer and not to revert back into the ladle at a later time.
(f) In the powder injection process, only when the initial momentum of particles is large enough can these participles completely penetrate the gas-liquid interface into the liquid metal; otherwise, they would remain in the bubble interior due to the impediment of bubble surface tension. Currently, some mathematical expressions have been developed to describe the particle penetration behavior at the gas-liquid interface.[27–31] According to Langberg *et al.*,[30] the particle penetration ratio is given by the following:

$$\eta_{\mathrm{p}} = 1 - \frac{\pi}{We_j}, \qquad [1]$$

where We_j is the Weber number of particle injection, which can be calculated by

$$We_j = \frac{m_{\mathrm{p}} u_{\mathrm{p}}}{\sigma D_0}, \qquad [2]$$

where m_{p} is the mass flow rate of powder injection, u_{p} is the particle velocity, σ is the gas-liquid surface tension, and D_0 is the characteristic diameter of powder tuyere. For the bottom powder injection in the industrial ladle, the minimum gas and powder flow rate are 50 NL/min and 1.5 kg/min, respectively, and the equivalent diameter of tuyere is 14.36 mm. Therefore, based on Eqs. [1] and [2], the present particle penetration η_{p} is greater than 0.9. In order to simplify the model, the η_{p} is initially set to 1 in the present model.

B. *CFD Model*

Based on the Euler-Euler approach, the mass and momentum balance equations are solved for each phase separately. The interaction forces among different phases in the present system are considered as momentum exchange source terms in the momentum equations.

Mass conservation:

$$\frac{\partial}{\partial t}(\alpha_k \rho_k \mathbf{u}_k) + \nabla \cdot (\alpha_k \rho_k \mathbf{u}_k) = S_k, \qquad [3]$$

where ρ_{k}, α_{k}, $\mathbf{u}_{\mathrm{k}}$, and S_{k} are the density, volume fraction, averaged velocity vector, and mass source term of liquid steel phase (k = l), gas phase (k = g), and powder particles (k = p), respectively. In Eq. [3], S_{l} (k = l) is zero for liquid phase, and S_{g} (k = g) and S_{p} (k = p) will be calculated by the PBM and SRM models, which will be described in detail in the subsequent section. Since the entire space domain is shared by these phases, the constraint condition $\alpha_{\mathrm{l}} + \alpha_{\mathrm{g}} + \alpha_{\mathrm{p}} = 1$ needs to be satisfied to enclose the model.

Momentum conservation:

$$\frac{\partial}{\partial t}(\alpha_k \rho_k \mathbf{u}_k) + \nabla \cdot (\alpha_k \rho_k \mathbf{u}_k \mathbf{u}_k) = -\alpha_k \nabla p + \nabla \cdot \left(\alpha_k \mu_{\mathrm{eff}} \left(\nabla \mathbf{u}_k + (\nabla \mathbf{u}_k)^T\right)\right) + \alpha_k \rho_k g + M_k, \qquad [4]$$

$$\mu_{\mathrm{eff}} = \mu_{\mathrm{l}} + \mu_{\mathrm{t}}, \qquad [5]$$

$$\mu_{\mathrm{t}} = C_{\mathrm{u}} \rho_{\mathrm{l}} \frac{k^2}{\varepsilon}, \qquad [6]$$

where g is the gravity acceleration; μ_{l}, μ_{t}, and μ_{eff} are the molecular viscosity, turbulent viscosity, and effective viscosity of liquid phase, respectively; p is the pressure, which is shared by all the phase; and M_{k} is the interaction force among the three phases, which can be expressed as

$$M_{\mathrm{g}} = F_{\mathrm{D}}^{\mathrm{g-l}} + F_{\mathrm{TD}}^{\mathrm{g-l}}, \qquad [7]$$

$$M_{\mathrm{p}} = F_{\mathrm{D}}^{\mathrm{p-l}} + F_{\mathrm{TD}}^{\mathrm{p-l}}, \qquad [8]$$

$$M_{\mathrm{l}} = -(M_{\mathrm{g}} + M_{\mathrm{p}}) \qquad [9]$$

where F_{D} and F_{TD} are drag and turbulent dispersion force, respectively, which have an important effect on the transport phenomena in gas-stirred systems, and the expressions are summarized in our recent publication.[14,32]

For the turbulence model, the bubble-induced turbulence produced during bubble floating has an important effect on the multiphase flow and is considered in present $k - \varepsilon$ turbulence equations. The importance and expression of the amended $k - \varepsilon$ turbulence model have been described in our recent publication[32] and will not be reproduced here.

C. *Population Balance Model of Powder Particles*

Population balance model of powder particles (PBM) is a complex and useful model to describe the size distribution of particles, including solid particles, bubbles, or droplets. The different phenomena, such as nucleation, growth, aggregation, and breakage, can be coupled into PBM to achieve more accurate prediction. Recently, the CFD-PBM coupled model has been adopted to describe the bubble flotation,[33,34] inclusion removal,[14,15] and slag foaming[35,36] in the relevant metallurgical field.

For the bottom powder injection process, the powder particle growth and removal behavior have a significant impact on the multiphase flow transport and desulfurization kinetics, and they are described by PBM:

$$\frac{\partial(\rho_{\mathrm{p}}\alpha_i)}{\partial t}+\nabla\cdot(\rho_{\mathrm{p}}\mathbf{u}_{\mathrm{p}}\alpha_i) = \rho_{\mathrm{p}}V_{\mathrm{i}}\left(\sum_{k=1}^{N}\sum_{j=1}^{N}\left(1-\frac{1}{2}\delta_{kj}\right)\beta_{kj}(V_k,V_j)n_k n_j\xi_{kj} - \sum_{j=i}^{N}\beta_{ij}(V_i,V_j)n_i n_j\right)+\rho_{\mathrm{p}}V_i S_i^{\mathrm{tot}} \quad i,j=0,1,\ldots,N-1 \tag{10}$$

$$\xi_{kj}=\begin{cases}\frac{V-V_{i-1}}{V_i-V_{i-1}} & \text{for } V_{i-1}<V_{\mathrm{ag}}<V_i\\ \frac{V_{i+1}-V_{\mathrm{ag}}}{V_{i+1}-V_i} & \text{for } V_i<V_{\mathrm{ag}}<V_{i+1}\\ 0 & \text{otherwise}\end{cases}, \tag{11}$$

where ρ_{p} and u_{p} are the density and velocity of the particle phase, respectively; δ_{kj} is assigned to 0 ($k \neq j$) or 1 ($k = j$); V_{ag} is the volume resulting from the aggregation of two particles; α_i is the volume fraction of particle size i; $\beta(V_i, V_j)$ represents the total coalescence rate between particles due to a variety of collision mechanisms; and S_i^{tot} represents the total removal rate from liquid steel due to a variety of removal mechanisms. These parameters can be written as

$$\beta_{ij}=\beta_{ij}^{\mathrm{TR}}+\beta_{ij}^{\mathrm{TS}}+\beta_{ij}^{\mathrm{S}}, \tag{12}$$

$$S_i^{\mathrm{tot}}=S_i^{\mathrm{Wall}}+S_i^{\mathrm{IF}}+S_i^{\mathrm{BIB}}+S_i^{\mathrm{BIR}}+S_i^{\mathrm{BIR}}+S_i^{\mathrm{Wake}}, \tag{13}$$

where β_{ij}^{TR}, β_{ij}^{TS}, and β_{ij}^{S} represent the particle coalescence rate due to turbulent random collision, shear collision in turbulent eddies, and Stokes buoyancy collision, respectively, and $S_i^{\mathrm{Wall}}, S_i^{\mathrm{IF}}, S_i^{\mathrm{BIB}}, S_i^{\mathrm{BIR}}, S_i^{\mathrm{BIS}}$ and S_i^{Wake} represent the mass source terms of particle removal due to wall adhesion, particle own floating near the slag-metal interface, bubble-particle buoyancy collision, bubble-particle turbulence random collision, bubble-particle turbulent shear collision, and bubble wake capture, respectively. The S_i^{Wall} is ignored in the present work because of its small influence on particle removal in the ladle.[14,15] The detailed expressions for particle coalescence and removal rate due to these mechanisms were studied and are described in our latest publication;[14] they will not be reproduced here.

D. *Species Mass Transport Equation*

1. *Species mass transport in liquid steel*

As shown in Figure 2, the species in liquid steel, such as aluminum, silicon, manganese, and sulfur, can be transferred simultaneously by molecular diffusion, liquid flow, and turbulent fluctuations and can also be removed from or produced into liquid steel due to chemical reactions. In the present model, these processes can be represented in the following form:

$$\frac{\partial}{\partial t}\left(\alpha_{\mathrm{l}}\rho\frac{[\mathrm{pct}\ Y_i]}{100}\right)+\nabla\cdot\left(\alpha_{\mathrm{l}}\rho\mathbf{u}_{\mathrm{l}}\frac{[\mathrm{pct}\ Y_i]}{100}\right) = \nabla\cdot\left(\alpha_{\mathrm{l}}\frac{\mu_{\mathrm{t}}}{Sc_{\mathrm{t}}}\left(\nabla\frac{[\mathrm{pct}\ Y_i]}{100}\right)\right)+S_i^{\mathrm{l-top}}+S_i^{\mathrm{l-p}}+S_i^{\mathrm{l-b}}, \tag{14}$$

where i is the species element in liquid steel, namely, S, Al, Si, Mn, and Fe; [Pct Y_i] is the local mass fraction of species i in liquid steel; Sc_t is the turbulent Schmidt number; $S_i^{\text{l-top}}$ is the source term due to chemical reactions on liquid steel top surface, which mainly include top slag-liquid steel interfacial reaction $S_i^{\text{l-slag}}$ and air-liquid steel interfacial reaction $S_i^{\text{l-air}}$ in top slag eyes; and $S_i^{\text{l-p}}$ and $S_i^{\text{l-b}}$represent mass source terms due to chemical reactions at the powder droplet-liquid steel interface and bubble-liquid steel interface. The reaction rates, $S_i^{\text{l-top}}$, $S_i^{\text{l-p}}$, and $S_i^{\text{l-b}}$ in Eq. [14] can be calculated by the SRM model, which will be described in detail in a later section.

2. *Species mass transport in the powder droplet*

In the present system, the mass transport of the species in the powder droplet can be represented in the following form:

$$\frac{\partial}{\partial t}\left(\alpha_{\mathrm{p}}\rho_{\mathrm{p}}\frac{(\mathrm{pct}\ Y_i)_{\mathrm{p}}}{100}\right)+\nabla\cdot\left(\alpha_{\mathrm{p}}\rho_{\mathrm{p}}u_{\mathrm{p}}\frac{(\mathrm{pct}\ Y_i)_{\mathrm{p}}}{100}\right) = \nabla\cdot\left(\alpha_{\mathrm{p}}\frac{\mu_{\mathrm{t}}}{Sc_{\mathrm{t}}}\left(\nabla\frac{(\mathrm{pct}\ Y_i)_{\mathrm{p}}}{100}\right)\right)+S_i^{\mathrm{p-b}}+S_i^{\mathrm{p-slag}}+S_i^{\mathrm{p\text{-}l}}, \tag{15}$$

where i is the species element in the powder droplet, namely, CaO, Al_2O_3, SiO_2, MnO, FeO, and CaS. $(\mathrm{pct}\,Y_i)_{\mathrm{p}}$ is the local mass fraction of species i in powder droplets. $S_i^{\text{p-b}}$ and $S_i^{\text{p-slag}}$ are the mass physical migration rate of species i from the powder droplet to the bubble and top slag due to their transport behavior, which can be given by

$$S_i^{\mathrm{p-b}}=S_{\mathrm{p-b},i}^{\mathrm{plume}}+S_{\mathrm{p-b},i}^{\mathrm{eye}}, \tag{16}$$

$$S_{\mathrm{p-b},i}^{\mathrm{plume}}=-\left(S_k^{\mathrm{BIB}}+S_k^{\mathrm{BIR}}+S_k^{\mathrm{BIS}}\right)\rho_{\mathrm{p}}V_{\mathrm{p}}(\mathrm{pct}\ Y_i)_{\mathrm{p}} \tag{17}$$

$$S_{\mathrm{p-b},i}^{\mathrm{eye}}=\rho_{\mathrm{g}}\alpha_{\mathrm{g}}(\mathrm{pct}\ Y_i)_{\mathrm{g}}, \tag{18}$$

where $S_{\text{p-b},i}^{\text{plume}}$ is the mass physical migration rate of species i from the powder to bubble due to the

powder-bubble collision and adhesion behavior in the bubbly plume zone. $S_{\text{p-b},i}^{\text{eye}}$ is the mass return rate from the bubble to powder droplet due to the rupture of the bubbles in the slag eye zone. S_k^{BIB}, S_k^{BIR}, and S_k^{BIS} represent powder particle adhesion rates due to bubble-particle buoyancy collision, turbulence random collision, and turbulent shear collision in the bubbly plume zone, respectively.

$$S_i^{\text{p-slag}} = -\left(S_k^{\text{Wake}} + S_k^{\text{IF}}\right)\rho_g V_g (\text{pct } Y_i)_p, \quad [19]$$

$$S_i^{\text{p-l}} = -S_i^{\text{l-p}}, \quad [20]$$

where S_k^{IF} and S_k^{Wake} represent the mass physical migration rate of species i from the powder droplet to top slag due to particle own floating and bubble wake capture near the slag-metal interface, which have also been described in our latest publication[14] and will not be reproduced here.

In Eq. [15], $S_i^{\text{p-l}}$ represents the mass chemical migration rate of species i from the powder to liquid steel due to the chemical reaction at the discrete droplet-liquid steel interface, which is the opposition relation with the term $S_i^{\text{l-p}}$ in Eq. [14].

3. *Species mass transport in the bubble*

In the bubbly plume zone, some dispersion powder particles will be adhered on the bubble surface due to particle-bubble collisions and become an integral part of the bubble, which, in turn, increase the weight of the bubble and affect the bubble floating behavior. Additionally, in the process of bubble floating, these particles adhered on the bubble will also contact and react with the liquid steel, which has an important effect on the desulfurization behavior. In the present work, the mass transport of the species in the bubble is complex and the related species conservation equation can be represented in the following form:

$$\frac{\partial}{\partial t}\left(\alpha_g \rho_g \frac{(\text{pct } Y_i)_g}{100}\right) + \nabla \cdot \left(\alpha_g \rho_g \mathbf{u}_g \frac{(\text{pct } Y_i)_g}{100}\right) = \nabla \cdot \left(\alpha_g \frac{\mu_t}{Sc_t}\left(\nabla \frac{(\text{pct } Y_i)_g}{100}\right)\right) + S_i^{\text{b-p}} + S_i^{\text{b-slag}} + S_i^{\text{b-l}}, \quad [21]$$

where i is the species element in the bubble, namely, Ar, CaO, Al_2O_3, SiO_2, MnO, FeO, and CaS. $(\text{pct } Y_i)_g$ is the local mass fraction of species i in the bubble. $S_i^{\text{b-p}}$ is the mass physical migration rate of species i from the bubble to powder droplet due to the interaction between the powder and bubble in the bubbly plume zone and slag eye zone, which is an opposition relation with the term $S_i^{\text{p-b}}$ in Eqs. [15] and [16].

$$S_i^{\text{b-p}} = -S_i^{\text{p-b}}, \quad [22]$$

where $S_i^{\text{b-slag}}$ represents the mass physical migration rate of element i from the bubble to top slag, because the droplets adhered on the bubble are removed into top slag with bubble rupture in the slag layer. The $S_i^{\text{b-slag}}$ can be expressed as follows:

$$S_i^{\text{b-slag}} = -\alpha_g \rho_g (\text{pct } Y_i)_g. \quad [23]$$

In Eq. [19], $S_i^{\text{b-l}}$ is the mass chemical migration rate of species i from the bubble to liquid steel due to the bubble-liquid steel reaction in the ladle, which is an opposition relation with the term $S_i^{\text{l-b}}$ in Eq. [14] and will be described in detail in the following SRM model.

$$S_i^{\text{b-l}} = -S_i^{\text{l-b}}. \quad [24]$$

E. *Multi-interface and Multicomponent SRM*

In the bottom powder injection process, there are four main chemical reaction places in the ladle, namely, top slag-liquid steel interface, air-liquid steel interface in slag eyes, dispersion powder droplet-liquid steel interface, and bubble-liquid steel interface, and the multicomponent reactions including Al, S, Si, Mn, Fe, and O are simultaneously involved in each interface.

1. *Top slag-liquid steel interface reactions*

In the bottom powder injection process in the ladle, the top slag-liquid steel reaction is one of the main chemical reaction places and has an important contribution on the desulfurization efficiency. At the top slag-liquid steel interface, the multiple reactions involving [Al], [Si], [Mn], [Fe], [O], and [S] are considered to occur simultaneously and the reaction rate of species i can be written as

$$S_i^{\text{l-slag}} = -\alpha_l \rho_l k_{\text{eff},i} \frac{A_{\text{cell}}}{100 V_{\text{cell}}}\left\{[\text{pct } Y_i] - \frac{(\text{pct } Y_i)}{L_i}\right\}, \quad [25]$$

where i is the species element in the liquid steel, namely, S, Al, Si, Mn, and Fe. $K_{\text{eff},i}$ characterizes the overall mass-transfer coefficient of species i from steel to slag. A_{cell} and V_{cell} are the local interface area and volume of cell on the liquid steel surface, respectively. L_i is the interfacial distribution ratio of element i at equilibrium, which represents the thermodynamics capacity of the slag-metal reaction and is a function of oxygen activity a_O^*. In order to close the equation, the oxygen kinetic balance equation of slag-metal reactions must be solved with a numerical iteration technique.

$$1.5\frac{S_{\text{Al}}^{\text{l-slag}}}{M_{\text{Al}}} + 2\frac{S_{\text{Si}}^{\text{l-slag}}}{M_{\text{Si}}} + \frac{S_{\text{Mn}}^{\text{l-slag}}}{M_{\text{Mn}}} = \frac{S_{\text{FeO}}^{\text{l-slag}}}{M_{\text{FeO}}} + \frac{S_{\text{S}}^{\text{l-slag}}}{M_{\text{S}}} + \frac{S_{\text{O}}^{\text{l-slag}}}{M_{\text{O}}}, \quad [26]$$

where M_i is the molecular weight of species i in liquid steel and slag. The detailed description of thermodynamic and kinetic parameters mentioned in Eqs. [25] and [26] have been clarified in our previous work.[20,21]

2. *Air-liquid steel interface reactions*

When liquid steel contacts with air at higher temperature, the oxygen will be absorbed from the atmosphere into steel and some elements in liquid steel will be

oxidized by dissolved oxygen. The oxidation reactions rate of species i in slag eyes can be written as

$$S_i^{\text{l-air}} = -k_{\text{m},i}\alpha_{\text{l}}\rho_{\text{l}}\frac{A_{\text{cell}}}{100V_{\text{cell}}}\{[\text{pct } Y_i] - [\text{pct } Y_i]^*\}, \quad [27]$$

where i is Al, Si, Mn, Fe, and C in liquid steel. $k_{\text{m},i}$ is the mass-transfer coefficient of species i in liquid steel, and [pct Y_i]* is the equilibrium concentration of species i at the air-liquid steel interface. In order to close the equation, the oxygen mass balance and carbon mass balance equations must be solved with a numerical iteration technique. The detailed description of these parameters was clarified in our previous work.[20]

3. *Powder droplet-liquid steel interface reaction*

In the ladle, similar to the top slag-liquid steel reaction, the multicomponent reactions involving Al, S, Si, Mn, Fe, and O will also occur simultaneously at the powder droplet-liquid steel interface. However, compared with the top slag-liquid steel reaction, the reaction rates of these fine powder droplets are more rapid due to the superior dynamic conditions and the sulfur concentration in these droplets will quickly increase to the saturation state. Then the solid phase of CaS will be produced, and the related thermodynamics and kinetics of desulfurization will vary, which, in turn, affect the desulfurization rate of powder. Based on the literature measured to date,[25,26] the solubility of CaS in the liquid slag can be approximated as

$$N_{\text{CaS,sat}} = 3.33 \text{ pct}\frac{(N_{\text{CaO}})}{(N_{\text{Al}_2\text{O}_3})} - 0.216 \text{ pct}, \quad [28]$$

where $N_{\text{CaS,sat}}$ is the molar saturation concentration of CaS in droplet. N_{CaO} and $N_{\text{Al}_2\text{O}_3}$ represent the molar concentrations of CaO and Al_2O_3 in the powder droplet, respectively.

Depending on whether the molar concentration of CaS in the powder droplet reaches saturation, the powder droplet-liquid steel interface reactions can be divided into the following two categories.

(1) Unsaturated state, *i.e.*, $N_{\text{CaS}} \le N_{\text{CaS,sat}}$

Before the molar concentration of CaO reaches the saturation state, the reaction rate of species i at the powder droplet-liquid steel interface can be written as

$$S_i^{\text{l-p}} = -\alpha_{\text{l}}\rho_{\text{l}}k_{\text{eff},i}^{\text{l-p}}\frac{6\alpha_{\text{p}}}{100d_{\text{p}}}\left\{[\text{pct } Y_i] - \frac{(\text{pct } Y_{\text{i}})_{\text{p}}}{L_i^{\text{l-p}}}\right\}, \quad [29]$$

where i is the species element involved reactions, namely, Al, Si, Mn, S, and Fe. [pct Y_i] and (pct Y_i)$_{\text{p}}$ are the local mass fraction of species i in the liquid steel and powder droplet, respectively. d_{p} is the diameter of the powder droplet, and $k_{\text{eff},i}$ characterizes the overall mass-transfer coefficient of species i from the steel to powder droplet, which is determined by the following expression:

$$k_{\text{eff},i}^{\text{l-p}} = \frac{k_{\text{m}}^{\text{l-p}}k_{\text{p}}L_i\rho_{\text{p}}}{k_{\text{p}}L_i\rho_{\text{p}} + \rho_{\text{l}}k_{\text{m}}^{\text{l-p}}}, \quad [30]$$

where $k_{\text{m}}^{\text{l-p}}$ and k_{p} are the mass-transfer coefficient of species i in the liquid steel and droplet, respectively. In a turbulent system, Kolmogorov microscale is a measurement of the smallest existing turbulence eddies, where the viscous forces begin to have a noticeable effect on the motion of the fluid. In our recent literature,[11] the Kolmogorov microscale has been predicted in the gas-stirred ladle, and it is usually greater than 30 μm at the gas flow rate from 50 to 200 NL/min. Therefore, in the bottom powder injection process, the fine powder particle is comparable to or smaller than the Kolmogorov microscale. Compared with the top slag-liquid steel interface, where mass transport behavior is mainly affected by turbulence motion and the influence of the molecular diffusion can be almost ignored, the mass transport behavior at the powder particle-liquid steel interface is mainly attributed to the joint effort of the turbulent diffusion and molecular viscous diffusion. Some studies[37–42] have reported the mass transport efficiency between liquid and fine particles, and according to Piero and Donald,[42] the mass-transfer efficiency $k_{\text{m}}^{\text{l-}p}$ from liquid to microparticles can be calculated by the following:

$$Sh = \frac{k_{\text{m}}^{\text{l-p}}d_{\text{p}}}{D} = 2 + 0.52Re_{\text{T}}^{0.52}Sc^{1/3}, \quad [31]$$

where Re_T, Sc, and Sh are the turbulent Reynolds number, Schmidt number, and Sherwood number.

$$Re_{\text{T}} = \left(\frac{\varepsilon d_{\text{p}}^4}{v^3}\right)^{1/3}, \quad [32]$$

$$Sc = \frac{v}{D}. \quad [33]$$

According to Eqs. [31] through [33], the mass-transfer efficiency $k_{\text{m}}^{\text{l-p}}$ from the liquid to droplet can be expressed as follows:

$$k_{\text{m}}^{\text{l-p}} = \frac{2D}{d_{\text{p}}} + 0.52\frac{Re_{\text{T}}^{0.52}\text{Sc}^{1/3}D}{d_{\text{p}}}. \quad [34]$$

In Eq. [30], k_{p} is the mass-transfer coefficient in the droplet interior, which can be given as follows:

$$k_{\text{p}} = \frac{2D_{\text{p}}}{d_{\text{p}}}, \quad [35]$$

where D_{p} is the diffusion coefficient of species i in the powder droplet.

In Eq. [29], $L_i^{\text{l-p}}$ is the interfacial distribution ratio of each element i between the droplet and liquid steel, which represents the thermodynamics capacity of the powder droplet-liquid steel reaction and can be expressed as a function of the interfacial oxygen activity $a_{\text{O,l-p}}^*$ at the powder droplet-liquid steel interface. Similar to the previous parameter $a_{\text{O,l-p}}^*$ must also be obtained by solving the oxygen kinetic balance Eq. [36] of powder droplet-liquid steel reactions with a numerical iteration technique.

$$1.5\frac{S_{Al}^{l-p}}{M_{Al}}+2\frac{S_{Si}^{l-p}}{M_{Si}}+\frac{S_{Mn}^{l-p}}{M_{Mn}}=\frac{S_{FeO}^{l-p}}{M_{FeO}}+\frac{S_{S}^{l-p}}{M_{S}}+\frac{S_{O}^{l-p}}{M_{O}}. \quad [36]$$

(2) Saturated state, *i.e.*, $N_{CaS} > N_{CaS,sat}$

In the process of bottom powder injection, once the CaS concentration in the powder droplet reaches saturation, the solid phase of CaS will be produced, and the desulfurization reaction can be expressed by the following reaction:

$$[S] + (CaO)=(CaS)_s+[O] \quad [37]$$

$$\log K_S = \log\frac{a_{O,l-p}^{*}}{a_S a_{CaO}} = -\frac{5629}{T}+1.654, \quad [38]$$

where K_S is the equilibrium constants, which are the activity ratios of the reactants and products at the powder droplet-liquid steel interface. a_{CaO} and a_S are the activities of CaO in the powder droplet and S in the liquid steel, respectively. In the present work, the related desulfurization rate after sulfur saturated in the droplet can be written as

$$S_S^{l-p} = -\alpha_l\rho_l k_m^{l-p}\frac{6\alpha_s}{100 d_s}\left\{[\text{pct } Y_S]-[\text{pct } Y_S]_{l-p}^{*}\right\}, \quad [39]$$

where $[\text{pct } Y_S]_{l\text{-}p}^{*}$ is the interface equilibrium concentration of element i at the liquid surface, which can be expressed as a function of $a_{O,l-p}^{*}$. According to Eq. [38], the related expressions are as follows:

$$[\text{pct } Y_S]_{l-p}^{*}=\frac{a_{O,l-p}^{*}}{K_S f_S a_{CaO}}. \quad [40]$$

Therefore, using Eqs. [29] and [36] through [39], the oxygen activity at the droplet-liquid steel interface can be obtained for the saturated state of CaS in the droplet, which, in turn, can give the reaction rate of each element $S_i^{l\text{-}p}$.

4. *Bubble-liquid steel interface reaction*

In the bubbly plume flow zone, a large amount of powder particles will be adhered to the bubble surface and become an integral part of the bubble, as shown in Figure 2. With the bubbles floating, these powder droplets will also contact and react with the liquid steel at the bubble-liquid steel interface. Similar to the powder droplet-liquid steel interface reaction, the bubble-liquid steel interface reaction can also be divided into two categories depending on whether the molar concentration of CaO reaches saturation in the powder droplet adhered on bubble.

(1) Unsaturated state, *i.e.*, $(N_{CaS})_g \le (N_{CaS,sat})_g$

In the present system, the powder droplets adhered to the bubbles are treated as a part of the bubble to simplify the model, but in fact, they are still physically separated from each other, *i.e.*, the Ar gas exists only inside the bubble, and the droplet component including (CaO), (Al_2O_3), (SiO_2), *etc.*, mainly exists on the bubble surface, as shown in Figure 3. Therefore, the real concentrations of component i involved in the bubble-liquid steel interfacial reaction $(\text{pct } Y_{Ar})_{g,\text{real}}$ can be express as follows:

$$(\text{pct } Y_i)_{g,real}=\frac{(\text{pct } Y_i)_g}{1-(\text{pct } Y_{Ar})_g} \quad [41]$$

where i is the species element involved reactions, namely, CaO, Al_2O_3, SiO_2, CaS, MnO, *etc.*, and $(\text{pct } Y_i)_g$ and $(\text{pct } Y_{Ar})_g$ are the local mass fractions of species i and argon in the bubble, respectively. The reaction rate of species i at the bubble-liquid steel interface can be written as

$$S_i^{l-b} = -\alpha_l\rho_l k_{eff,i}^{l-b}\frac{6f\alpha_g\rho_g\left(1-\frac{(\text{pct } Y_{Ar})_g}{100}\right)}{100\rho_p d_p} \times\left\{[\text{pct } Y_i]-\frac{(\text{pct } Y_i)_{g,real}}{L_i^{l-b}}\right\}, \quad [42]$$

where f represents the ratio of the effective contact area between the adhered droplet and liquid steel. As shown in Figure 3, part of the droplet volume will be exposed to the outside of the bubble and the other part will be embedded inside the bubble. In this article, in order to simplify the model, f was uniformly set to 0.5. ρ_g is the density of the bubble after adhering powder particles and can be calculated using the following expression:

$$\rho_g = \left(1-(\text{pct } Y_{Ar})_g\right)\rho_p+(\text{pct } Y_{Ar})_g\rho_{Ar}. \quad [43]$$

In Eq. [42], $k_{eff,i}^{l\text{-}b}$ represents the mass-transfer coefficient at the bubble-steel liquid interface, which can be given as follows:

$$k_{eff,i}^{l-b}=\frac{k_m^{l-b}k_p L_i\rho_p}{k_p L_i\rho_p+\rho_l k_m^{l-b}}. \quad [44]$$

In the bubbly plume zone, the bubbles will appear in random motion due to the influence of turbulent eddies, which will affect the mass transport behavior between bubble-liquid steel; therefore, the mass-transfer coefficient $k_{eff,i}^{l\text{-}b}$ can be calculated through the Komogorov theory of isotropic turbulence as follows:

$$k_m^{l-b}=cD_{m,i}^{0.5}\left(\frac{\varepsilon_l}{\nu}\right)^{0.25}, \quad [45]$$

where c is 0.4 for this work based on Lamont and Scott.[43] The $D_{m,i}$ values are diffusion coefficients of species i in liquid steel. k_p is the mass-transfer coefficient of species i in the powder droplet adhered on the bubble, which can be obtained by Eq. [33].

In Eq. [42], $L_i^{l\text{-}b}$ is the interfacial distribution ratio of each element i between the bubble and liquid steel and can be expressed as a function of the interfacial oxygen activity $a_{O,l\text{-}b}^{*}$, which must be obtained by

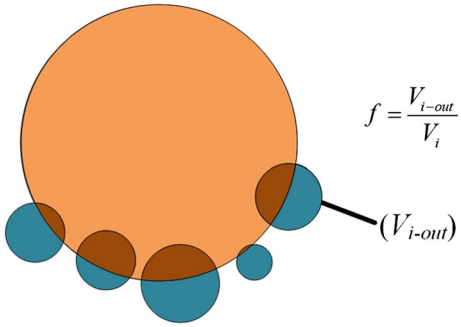

Fig. 3—Schematic diagram of powder particle-bubble collision and adhesion.

solving the following oxygen kinetic balance of bubble-metal reactions with a numerical iteration technique.

$$1.5\frac{S_{\mathrm{Al}}^{\mathrm{l-b}}}{M_{\mathrm{Al}}}+2\frac{S_{\mathrm{Si}}^{\mathrm{l-b}}}{M_{\mathrm{Si}}}+\frac{S_{\mathrm{Mn}}^{\mathrm{l-b}}}{M_{\mathrm{Mn}}}=\frac{S_{\mathrm{FeO}}^{\mathrm{l-b}}}{M_{\mathrm{FeO}}}+\frac{S_{\mathrm{S}}^{\mathrm{l-b}}}{M_{\mathrm{S}}}+\frac{S_{\mathrm{O}}^{\mathrm{l-b}}}{M_{\mathrm{O}}}. \quad [46]$$

(2) Saturated state, *i.e.*, $(N_{\mathrm{CaS}})_{\mathrm{g}} > (N_{\mathrm{CaS,sat}})_{\mathrm{g}}$

In the bubble-liquid steel reaction process, once the product CaS concentration in the powder droplet, which is adhered on the bubble, reaches saturation, the solid phase of CaS will be produced, and the desulfurization rate can be expressed by the following expression:

$$S_{\mathrm{S}}^{\mathrm{l-b}}=\alpha_{\mathrm{l}}\rho_{\mathrm{l}}k_{\mathrm{m},i}\frac{6f\alpha_{\mathrm{g}}\rho_{\mathrm{g}}\left(1-\frac{(\mathrm{pct}\ Y_{\mathrm{Ar}})_{\mathrm{g}}}{100}\right)}{100\rho_{\mathrm{p}}d_{\mathrm{p}}}\{[\mathrm{pct}\ Y_{\mathrm{S}}]-[\mathrm{pct}\ Y_{\mathrm{S}}]_{\mathrm{l-b}}^{*}\}, \quad [47]$$

where $[\mathrm{pct}\,Y_{\mathrm{S}}]_{\mathrm{l\text{-}b}}^{*}$ is the equilibrium concentration of sulfur at the bubble-liquid interface, which can be expressed as a function of $a_{\mathrm{O,l\text{-}b}}^{*}$:

$$[\mathrm{pct}\ Y_{\mathrm{S}}]_{\mathrm{l-b}}^{*}=\frac{a_{\mathrm{O}}^{*}}{K_{\mathrm{S}}f_{\mathrm{S}}a_{\mathrm{CaO,g}}}. \quad [48]$$

Therefore, using Eqs. [42] and [46] through [48], the oxygen activity at the bubble-liquid steel interface can be obtained for the saturated state of CaS, which, in turn, can give the reaction rate of each element $S_i^{\mathrm{l\text{-}b}}$.

III. EXPERIMENTAL AND NUMERICAL SCHEME

A. *Experimental Scheme*

To validate and correct the model, three runs of hot tests were carried out in the 2-t induction furnace with bottom powder injection. In the refining process, a fixed number of alloys and specially designed synthetic top slags was introduced into the liquid steel for deoxidization and composition adjustment of the liquid steel. The chemical compositions of the top slag and powder are shown in Table I. Two minutes later, the samples of liquid steel were taken to analyze their chemical compositions as the initial conditions before the start of the bottom powder injection, as shown in Table II. Then the 600-mesh powder made by grinding the slag was injected into liquid steel through homemade powder injection equipment and bottom slot plugs located in the middle of the 2-t furnace bottom, and the size distribution of the 600-mesh powder is shown in Figure 4, which was measured by means of the electric sensing zone method (Coulter counter, Omec Co., Ltd, Zhuhai, China). The homemade experimental apparatus is shown in Figure 5. The powder injection rate was 0.75 kg/min, and the total powder injection time was 6 minutes. Another two samples of liquid steel were taken out at an interval of 3 minutes to analyze the composition; the related detailed parameters are given in Tables III and IV. Figure 6 shows the experimental photos of the bottom powder injection process in the 2-t medium frequency induction furnace.

B. *Numerical Scheme*

In the present work, the CFD-PBM-SRM coupled model was solved using the commercial CFD software fluent 12.0 combined with a user-defined function, to describe the multiphase transport behavior and reaction kinetics of the bottom powder injection process in the 2-t induction furnace. The dimensions of the 2-t induction furnace and other parameters are listed in Table V. Figure 7 shows the mesh and boundary conditions of the water model ladle, and due to the symmetry of the flow, only half of the geometric model was built as a computational domain. The bottom and side walls were set as no-slip solid walls, and the standard wall function was used to model the turbulence characteristics in the near wall region. The velocity inlet was used for gas blowing and powder injection at the bottom tuyeres, and the velocity of the powder particle was assumed to be the same as the gas velocity at the bottom slot according to our previous group research.[44] The initial diameter distribution of the powder particle at the velocity inlet was set based on Figure 4. A flat surface was assumed at the top surface. Two different grids of the model were generated with the increasing number of control cell volume (214,425 and 160,743). Simulation was performed on both grids using the gas flow rate of 50 NL/min and powder injection rate of 0.75 kg/min. The convergence of the solution in both cases was verified, and there were no significant differences in the predicted results. Therefore, for all the subsequent simulations, the mesh consisting of 160,743 control volumes was used.

The slag eyes are formed on the liquid surface due to the action of inert gas bubbling. The shape of slag eyes is circular, and the circle center of the slag eye is determined on the position of maximum gas volume fraction of each bubbly plume in the liquid surface. The circle radius r_{e} of the slag eye could be calculated by the following expression[45,46]:

$$r_{\mathrm{e}}=0.56H\left(-0.76\left(\frac{Q_{\mathrm{g}}}{g^{0.5}H^{2.5}}\right)^{0.4}+7.15\left(1-\frac{\rho_{\mathrm{s}}}{\rho_{\mathrm{l}}}\right)^{-0.5}\left(\frac{Q_{\mathrm{g}}}{g^{0.5}H^{2.5}}\right)^{0.73}\left(\frac{h}{H}\right)^{-0.5}\right), \quad [49]$$

Table I. Chemical Composition of Top Slag and Powder Used in 2-t Medium Frequency Induction Furnace

(Al_2O_3)	(SiO_2)	(CaO)	(S)	(CaF)	(FeO)	(MnO)
21.32 pct	6.12 pct	57.62 pct	0.08 pct	13.07 pct	1.23 pct	0.12 pct

Table II. Chemical Composition of Liquid Steel at the Initial Time in 2-t Furnace

	Composition in Steel (Pct)					
	[Al]	[Si]	[Mn]	[C]	[S]	Temperature [K (°C)]
Run 1	0.048	0.258	0.673	0.372	0.0323	1836 K (1563 °C)
Run 2	0.063	0.226	0.627	0.305	0.0267	1830 K (1557 °C)
Run 3	0.052	0.252	0.608	0.354	0.0238	1828 K (1555 °C)

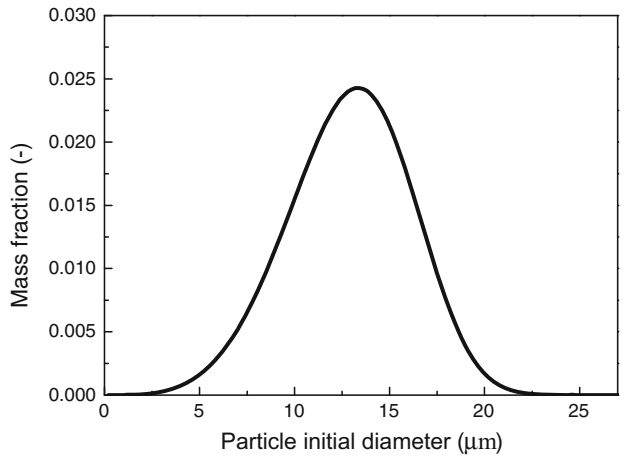

Fig. 4—Size distribution of the 600-mesh powder particle.

where Q_g is the gas flow rate (m^3/s) and h and H are the heights of liquid steel and slag layer, respectively.

Figure 8 shows schematically overall the solution in the framework of the CFD-PBM-SRM coupled model. In the CFD model, the local flow field, volume fraction, and turbulent energy dissipation rate were obtained by solving the mass, momentum, and $k-\varepsilon$ turbulent equations, respectively, and the species mass transport model was solved to obtain the local content distribution and overall removal ratio of each species in the ladle. Then the related parameters were transferred into PBM and SRM. In the PBM model, the particle-particle collision rate, particle-bubble adhesion rate, particle removal rate, and particle size distribution could be obtained and then transferred into CFD and SRM to update the source terms of each equation for the next time-step. In the SRM model, the chemical reaction rates S_i at the top slag-liquid steel interface, air-liquid steel interface, powder droplet-liquid steel interface, and bubble-liquid steel interface were calculated and transferred into CFD to update the source terms of the species transport equation for the next time-step. In the present model, the stable convergence needed to be guaranteed in each time-step in order to obtain more accurate predicted results, and the time-step of 0.25 was selected. The iteration residual was set to fall below 1×10^{-3} at each time-step. The simulations were carried out on the server computer (10 cores, 2.55 GHz, and 16 GB memory) and lasted about 35 hours for each case.

IV. MODEL VALIDATION

In the bottom powder injection process, the multiphase flow transport and chemical reactions behavior affect significantly desulfurization efficiency and effectiveness and need to be accurately described and predicted. In our previous work,[17,18,29] by the CFD model, the predicted bubbly plume flow, including the gas volume fraction, liquid velocity, and turbulent kinetic energy, was validated against experimental data,[29] and by the CFD-SRM coupled model, the predicted multicomponent simultaneous reaction at the top slag-liquid steel interface in the ladle agreed well with the measured data.[17,18] In the present work, the CFD-PBM-SRM coupled model to predict the desulfurization reaction behavior in the bottom powder injection process was verified with a hot experiment in the 2-t induction furnace. The hot experimental scheme and experimental results were described in detail in Section III.

A. *Multiphase Flow*

Figure 9 shows the predicted gas and powder volume fraction and the flow pattern of liquid steel in the 2-t furnace. The gas flow rate was 50 NL/min, and the powder injection rate was 0.75 kg/min. α_g and α_p are the volume fractions of the gas phase and powder particle phase, respectively. It should be noted that the legends in the figures consist of level number and real value. As shown in Figure 9(a), the left side of the legend indicates the level number from 1 to 10, and correspondingly, the right side of the legend represents the true value for each level. It can be observed from this figure that during bubble and powder particle floating, the bubble-powder flow in the center of the induction furnace produces dispersion along the radial direction. The upwelling steel flow forming in the bubbly plume zone turns horizontally toward the sidewall in the vicinity of the surface

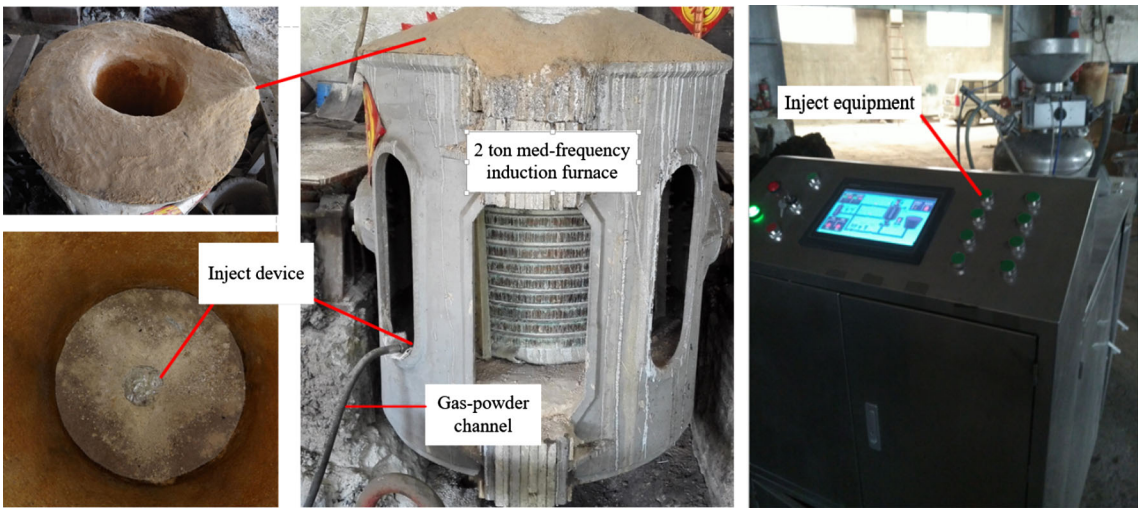

Fig. 5—Experimental apparatus of bottom powder injection for the 2-t medium frequency induction furnace.

Table III. Chemical Composition of Liquid Steel in 3 min After the Start of Bottom Powder Injection in 2-t Furnace

	Composition in Steel (Pct)					
	[Al]	[Si]	[Mn]	[C]	[S]	Temperature [K (°C)]
Run 1	0.028	0.256	0.671	0.332	0.0161	1834 K (1561 °C)
Run 2	0.039	0.226	0.628	0.280	0.0108	1827 K (1554 °C)
Run 3	0.032	0.250	0.060	0.312	0.0105	1827 K (1554 °C)

Table IV. Chemical Composition of Liquid Steel in 6 min After the Start of Bottom Powder Injection in 2-t Furnace

	Composition in Steel (Pct)					
	[Al]	[Si]	[Mn]	[C]	[S]	Temperature [K (°C)]
Run 1	0.015	0.252	0.673	0.308	0.0117	1833 K (1560 °C)
Run 2	0.025	0.212	0.626	0.245	0.0084	1826 K (1553 °C)
Run 3	0.024	0.247	0.610	0.289	0.0057	1824 K (1551 °C)

Fig. 6—Experimental photos of the bottom powder injection process in the 2-t medium frequency induction furnace.

and descends further along the wall. As a result, the circulations form in the entire furnace. Furthermore, unlike the bubble motion, most of the powder particles could not directly escape into air at the liquid surface, and they will gradually disperse in the whole furnace following the liquid steel flow, as shown in Figure 9(b).

B. *Desulfurization Reaction Kinetics*

In the bottom powder injection process, there are four main chemical reaction places in the ladle, namely, top slag-liquid steel interface, air-liquid steel interface in the slag eye, dispersion particle-liquid steel interface, and bubble-liquid steel interface.

Table V. Dimensions of 2-t Induction Furnace and Other Parameters

Diameter of furnace	690 mm
Height of furnace	750 mm
Argon gas flow rate	50 NL/min
Density of liquid steel	7100 kg/m^3
Surface tension between molten steel and argon gas	1.4 N/m
Density of gas	0.865 kg/m^3
Molecular viscosity of molten steel	0.0055 Pa s

1. *Powder particle-liquid steel interface reaction*

Figure 10 illustrates the predicted desulfurization reaction molar rate at the powder droplet-liquid steel interface in the 2-t furnace. In this figure, the gas flow rate was 50 NL/min and the powder injection rate was 0.75 kg/min. The component concentrations of the liquid steel, top slag, and powder particle are given in Tables I and II. $n^{\text{l-p}}_{\text{S,melt}}$ and $n^{\text{l-p}}_{\text{S,solid}}$ represent the desulfurization molar rates when the desulfurization products of CaS are liquid phase and solid phase, which can be calculated by Eqs. [29] through [40].

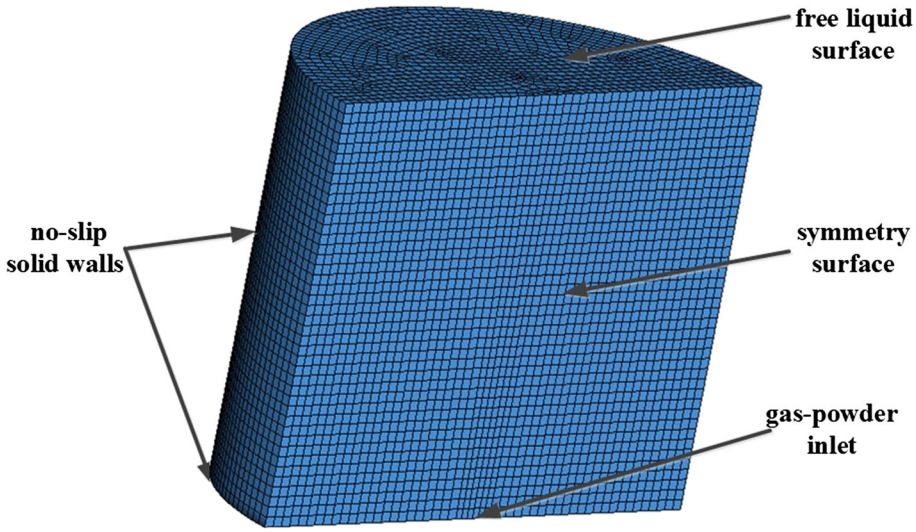

Fig. 7—Mesh and boundary conditions of the 2-t induction furnace.

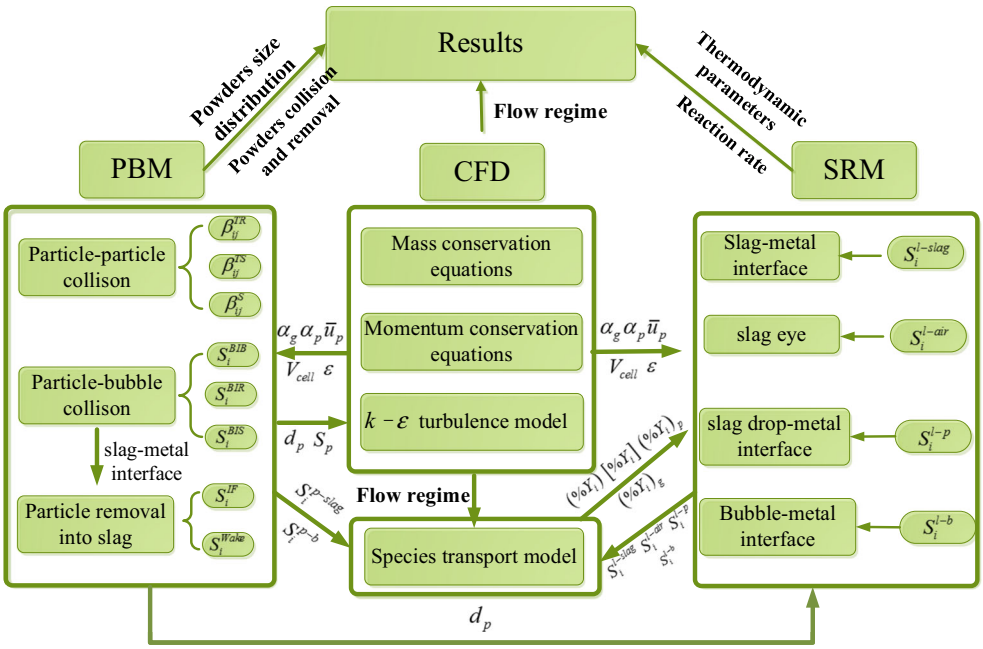

Fig. 8—Overall solution schematic of the CFD-PBM-SRM coupled model.

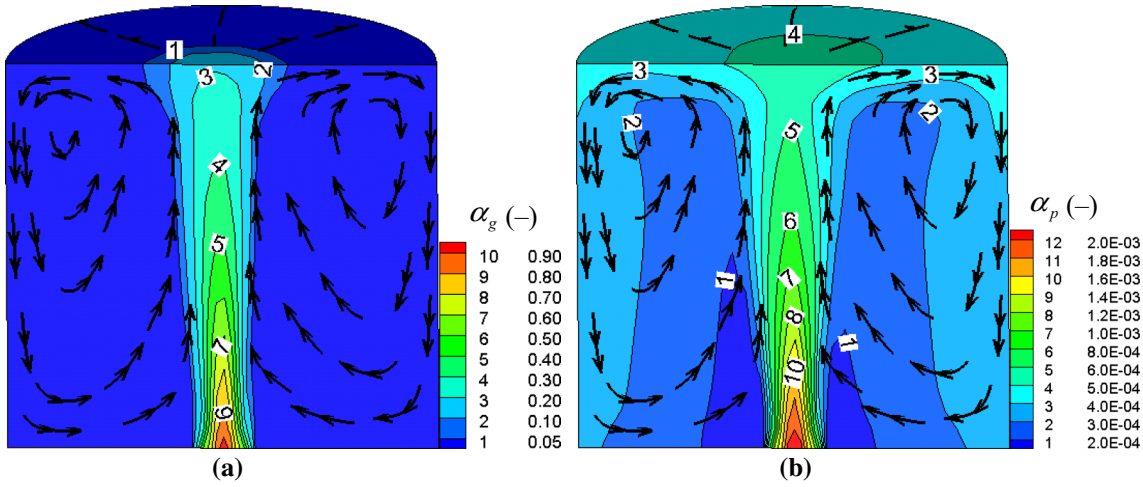

Fig. 9—Predicted (*a*) gas volume fraction and (*b*) powder volume fraction in the bottom powder injection process in the 2-t induction furnace.

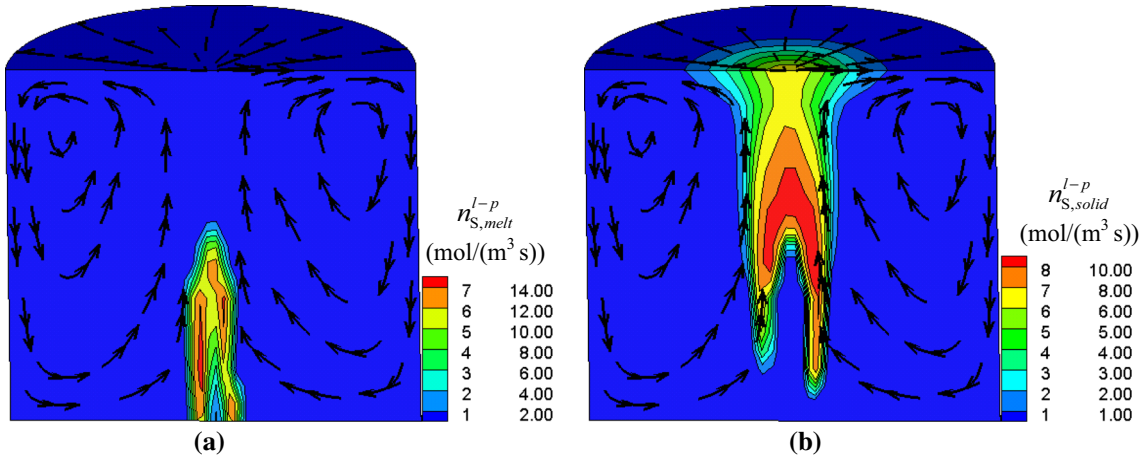

Fig. 10—Predicted contour map of the sulfur reaction molar rate at the powder droplet-liquid steel interface: (*a*) $n^{l-p}_{S,melt}$ and (*b*) $n^{l-p}_{S,solid}$.

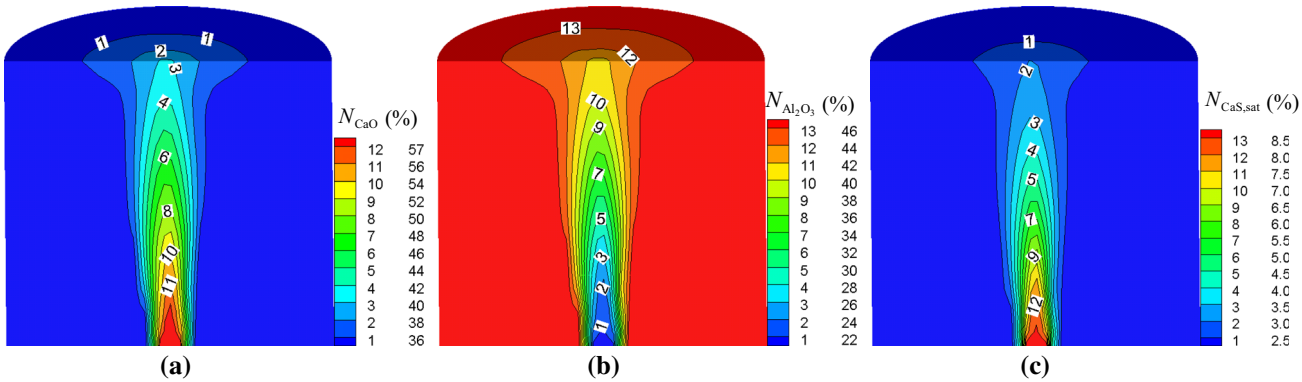

Fig. 11—Predicted contour map of (*a*) CaO molar concentration, (*b*) Al_2O_3 molar concentration, and (*c*) CaS saturation molar concentration in the powder droplet.

From Figure 10, it can be seen that in the vicinity of the bottom slot plugs, the desulfurization product CaS was liquid phase, while in the upper region of the furnace, the desulfurization product CaS was solid phase. This is mainly because, as the refining powder was injected into liquid steel, the chemical reactions strongly took place between the fine powder droplet and liquid steel, and the liquid phase product CaS and Al_2O_3 concentrations rapidly increased while the CaO concentration in the droplet decreased, as shown in Figure 11. In this figure, N_{CaO} and $N_{Al_2O_3}$ represent the molar fractions of CaO and Al_2O_3 in the powder droplet,

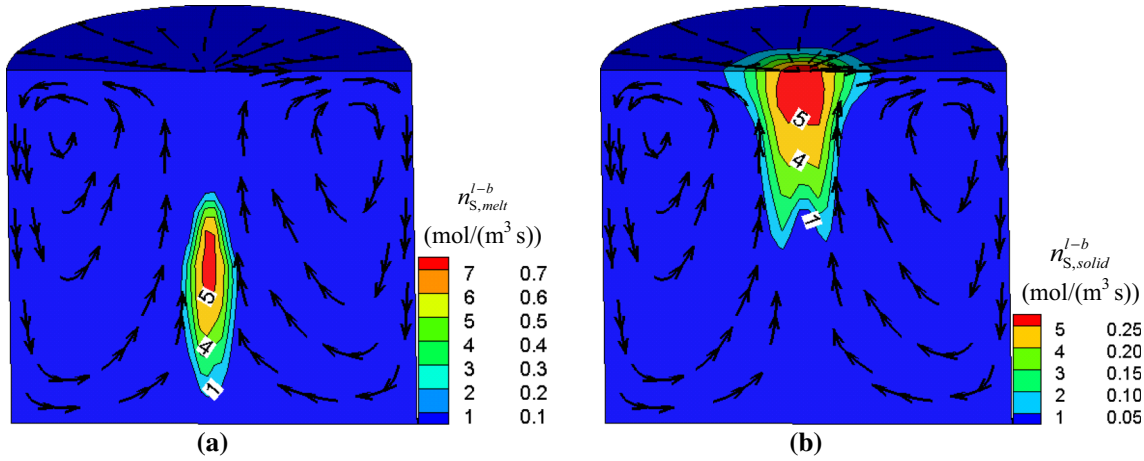

Fig. 12—Predicted contour map of the sulfur reaction molar rate at the bubble-liquid steel interface: (*a*) $n^{l-b}_{S,melt}$ and (*b*) $n^{l-b}_{S,solid}$.

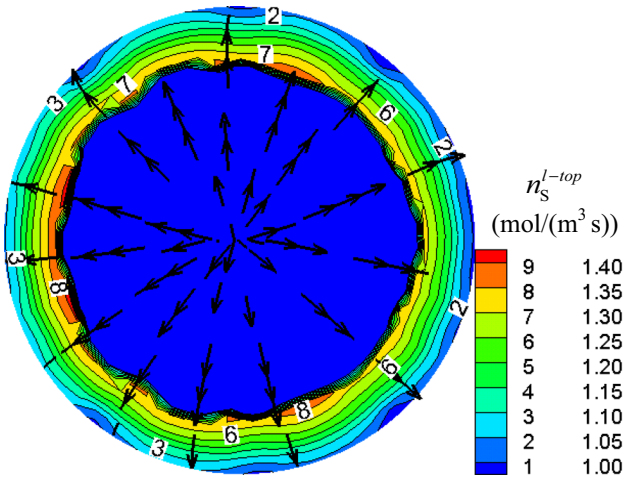

Fig. 13—Predicted sulfur reaction molar rate at the top slag-liquid steel interface in the 2-t furnace with bottom powder injection.

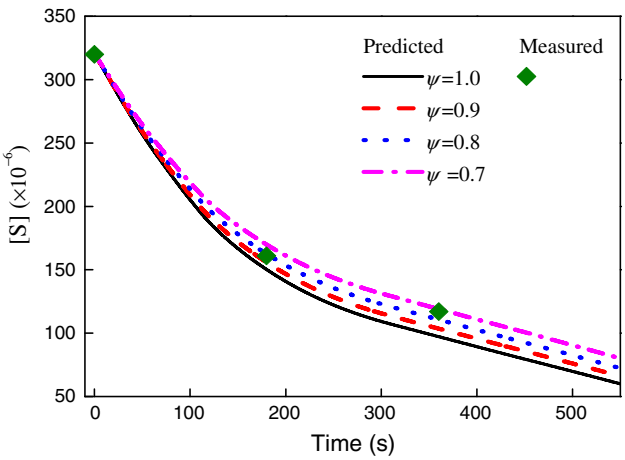

Fig. 14—Predicted and measured sulfur contents with time in the 2-t furnace with different parameters.

respectively. $N_{CaS,sat}$ is the molar saturation fraction of CaS in the droplet, which can be calculated by N_{CaO} and $N_{Al_2O_3}$ according to Eq. [28]. As seen in Figure 11(c), the

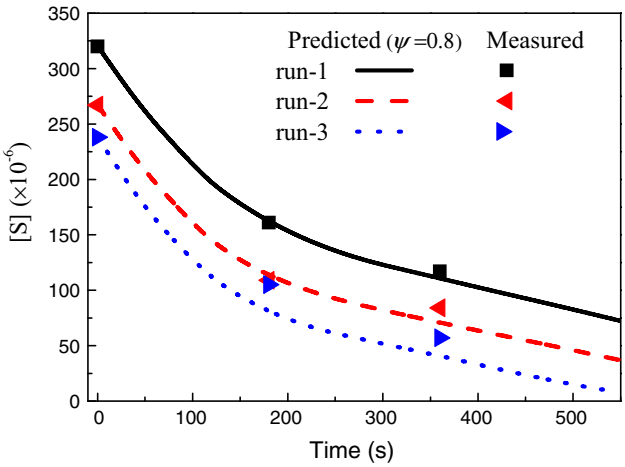

Fig. 15—Predicted and measured sulfur contents with time in the 2-t furnace for different initial components of liquid steel.

solubility of CaS in the slag droplet would decrease rapidly with the droplets floating. Once the sulfur saturated, *i.e.*, $N_{CaS} > N_{CaS,sat}$, the solid phase of CaS would be produced and the related thermodynamics and kinetics of desulfurization would vary, which, in turn, would reduce the desulfurization rate of powder.

2. *Bubble-liquid steel interface reaction*

In the bubbly plume zone, a large amount of powder particles would adhere to the bubble surface and become an integral part of the bubbles. With the bubbles floating, these powder droplets adhered on bubbles would also contact and react with the liquid steel.

Figure 12 shows the predicted desulfurization reaction molar rate at the bubble-liquid steel interface in the 2-t furnace. $n^{l-b}_{S,melt}$ and $n^{l-b}_{S,solid}$ represent the desulfurization molar rate when the desulfurization product CaS is liquid phase and solid phase, which can be calculated by Eqs. [41] through [48]. It can be found from this figure that similar to the powder droplet-liquid steel interface reaction, in the lower region of the bubbly plume zone, the desulfurization product CaS is liquid

phase, while in the upper region of the bubbly plume zone, the desulfurization product CaS is solid phase. Furthermore, compared with the powder-liquid steel interface reactions, the bubble-liquid steel interface reaction rate is obviously smaller, because the contact specific surface and time between the bubble and liquid steel are far lower than those between the dispersion particles and liquid steel.

3. *Top slag-liquid steel interface reactions*

Figure 13 shows the predicted desulfurization reaction molar rate $n_S^{l\text{-top}}$ at the top slag-metal interface in the 2-t furnace with bottom powder injection. In this figure, the gas flow rate is 50 NL/min, the powder injection rate is 0.75 kg/min, the height ratio of the top slag layer and liquid steel is 0.04, and the component concentrations are given in Tables I and II. From this figure, it can be found that the slag eye is formed as a large region where the top slag is pushed to the periphery of the furnace by the action of inert gas bubbling, and outside the slag eye zone, the sulfur will be removed from liquid steel into slag. The reaction molar rate gradually decreases along the radial direction from the slag eyes to the side wall. Furthermore, the molar rate of the desulfurization reaction at the top slag-liquid steel interface is significantly lower than that at the powder-liquid steel interface and gradually decreases along the radial direction.

C. *Model Validation*

In the powder injection process, there are always some powder particles that cannot penetrate the gas-liquid interface into the liquid metal and remain in the bubble interior due to the impediment of bubble surface tension. Therefore, the parameter ψ is proposed to represent the effective penetration of powder particles. Figure 14 shows the effect of different values of ψ on the sulfur removal rate and the comparison between the predicted results and measured data in the 2-t furnace. In this figure, the total gas flow rate is 50 NL/min, the powder injection rate is 0.75 kg/min, and the height ratio of top slag layer and liquid steel is 0.04. The initial compositions of slag and liquid steel are shown in Tables I and II. From this figure, it can be observed that with the decrease of coefficient ψ, the predicted removal rate of sulfur becomes slow, and as the ψ is 0.8, the predicted sulfur content agrees well with the measured data.

Figure 15 compares the predicted removal rate of sulfur with the measured data under different initial components of liquid steel, namely, runs 1, 2, and 3 in Tables II, III, and IV, respectively, and the coefficient ψ is chosen to be 0.8. It can be seen from this figure that the predicted sulfur contents agree well with the measured data under different initial conditions, and it implies that the present CFD-PBM-SRM coupled model could reasonably predict the desulfurization kinetics behavior in the bottom powder injection process, which provides a theoretical basis for further research to investigate desulfurization efficiency and effectiveness under different kinetic conditions in the industrial ladle.

V. CONCLUSIONS

A CFD-PBM-SRM coupled model has been proposed to describe the multiphase flow behavior and reaction kinetics in the bottom powder injection process, and some new and important phenomena and mechanisms were presented. Model validation was carried out using hot tests in the 2-t medium frequency induction furnace with bottom powder injection.

1. The bubble-powder flow produces dispersion along the radial direction in the 2-t furnace, and a circulation pattern of liquid steel forms in the entire furnace. The powder particles will be gradually dispersed in the entire furnace.
2. In the vicinity of bottom slot plugs, the desulfurization product CaS is liquid phase, while in the upper region of the furnace, the desulfurization product CaS is solid phase. The desulfurization rate of the powder-liquid steel interface reaction is greater than that of the bubble-liquid steel interface and top slag-liquid steel interface reactions in the 2-t furnace.
3. The sulfur contents predicted by the present model agree well with the measured data in the 2-t furnace with bottom powder injection, and the current model could reasonably predict the desulfurization kinetics in the bottom powder injection process.

ACKNOWLEDGMENTS

The authors express thanks to the National Natural Science Foundation of China (Grant Nos. U1560208 and 51604071) for supporting this work.

NOMENCLATURE

D_0	Characteristic diameter of powder tuyere (m)
D_p	Diffusion coefficient of powder droplet (m^2/s)
d_p	Diameter of powder particle (m)
F_D	Drag force per unit volume (N/m^3)
F_{TD}	Turbulent dispersion force per unit volume (N/m^3)
g	Acceleration due to gravity (m^2/s)
k_l	Liquid turbulent kinetic energy (m^2/s^2)
k_m^{l-p}, k_p	Mass-transfer coefficient in liquid steel and droplet (m/s)
L_i, L_i^{l-p}	Distribution ratio of element i at liquid steel-slag interface and liquid steel-powder particle interface

M_k	Interphase momentum exchange term (N/m^3)
m_p	Mass flow rate of particle injection (kg/min)
$N_{CaS,sat}$	Molar saturation fraction of CaS in powder droplet
N_{CaO}, $N_{Al_2O_3}$	Molar fraction of CaO and Al_2O_3 in powder droplet
Re_T	Particle turbulent Reynolds number
S_p	Total removal rate of powder particle due to a variety of removal mechanisms ($kg/(m^3\ s)$)
$S_i^{Wall}, S_i^F, S_i^{BF}, S_i^{BT}, S_i^{BS}, S_i^{Wake}$	Powder particle removal rate due to wall adhesion and inclusions own floating, bubble-particle floating collision, bubble-particle turbulence random collision, bubble-powder turbulent shear collision, and bubble wake capture ($kg/(m^3 s)$)
$S_i^{l-slag}, S_i^{l-air}, S_i^{l-p}, S_i^{l-b}$	Reaction rate of species i at the liquid steel-top slag interface, liquid steel-air interface, liquid steel-powder particle interface, and liquid steel-bubble interface ($kg/(m^3\ s)$)
$S_i^{p-b}, S_i^{p-slag}, S_i^{b-slag}$	Physical migration rate of species i at particle-bubble interface, particle-top slag interface, and bubble-top slag interface ($kg/(m^3\ s)$)
Sc	Schmidt number
Sh	Sherwood number
$\mathbf{u}_l$, $\mathbf{u}_g$, $\mathbf{u}_p$	Liquid, gas, and powder particle velocities (m/s)
V_{cell}	Grid cell volume (m^3)
[pct Y_i], (pct Y_i)$_p$, (pct Y_i)$_g$	Local mass fraction of species i in liquid steel, powder droplets, and bubble
α_g, α_p	Volume fraction of gas and powder particle
β	Total coalescence rate between particles due to a variety of collision mechanisms (m^3/s)
β_{ij}^{TR}, β_{ij}^{TS}, β_{ij}^{S}	Particle coalescence rate due to turbulent random collision, shear collision in turbulent eddies, and Stokes collision (m^3/s)
ρ_l, ρ_g, ρ_p	Liquid, gas, and powder particle density (kg/m^3)
μ_l, μ_t, μ_{eff}	Liquid molecular viscosity, turbulent viscosity, and effective viscosity (kg/(m s))
ε	Turbulent dissipation rate (m^2/s^3)

SUBSCRIPT

g Gas phase
l Liquid phase
p Powder particle phase

REFERENCES

1. M.Y. Zhu, J.A. Zhou, S.S. Pan, and J. Sha: Chinese Patent CN200510047980.1, 2006.
2. M.Y. Zhu, Z.F. Chen, and W.T. Lou: Chinese Patent CN201210012782.1, 2014.
3. M.Y. Zhu, Z.F. Chen, and W.T. Lou: Chinese Patent CN201310207525.8, 2014.
4. Z.F. Chen and M.Y. Zhu: *Metall. Mater. Trans. B*, 2014, vol. 45B, pp. 1695–1705.
5. N. Ei-Kaddah and J. Sezekely: *Ironmaking Steelmaking*, 1981, vol. 8 (6), pp. 269–78.
6. S. Ohguchi and D.G.C. Robertson: *Ironmaking Steelmaking*, 1984, vol. 11 (5), pp. 263–72.
7. V. Seshadri, C.A.D. Silva, I.A.D. Silva, and P.V. Kruger: *ISIJ Int.*, 1997, vol. 37 (1), pp. 21–30.
8. J.H. Wei, S.J. Zhu, and N.W. Yu: *Acta Metall. Sin.*, 1998, vol. 34 (5), pp. 497–505.
9. Z.S. Zou, Y.S. Zou, L.B. Zhang, and N. Wang: *ISIJ Int.*, 2001, vol. 41 (S), pp. 66–69.
10. C.Y. Zhu, P.J. Chen, G.Q. Li, X.Y. Luo, and W. Zheng: *ISIJ Int.*, 2016, vol. 56, pp. 1368–77.
11. M. Andersson, M. Hallberg, L. Jonsson, and P. Jönsson: *Ironmaking Steelmaking*, 2002, vol. 29, pp. 224–32.
12. L. Jonsson, S.C. Du, and P. Jönsson: *ISIJ Int.*, 1998, vol. 38, pp. 260–67.
13. M.A.T. Andersson, L.T.I. Jonsson, and P.G.P. Jönsson: *ISIJ Int.*, 2000, vol. 40, pp. 1080–88.
14. W.T. Lou and M.Y. Zhu: *Metall. Mater. Trans. B*, 2013, vol. 44B, pp. 762–82.
15. W.T. Lou and M.Y. Zhu: *ISIJ Int.*, 2014, vol. 54B (1), pp. 9–18.
16. T. Shoji, T. Mitsuo, Y. Hitta *et al.*: *Tetsu-to-Hagané*, 1982, vol. 68 (6), pp. 609–17.
17. S. Mukawa: *Tetsu-to-Hagané*, 2004, vol. 90 (6), pp. 408–13.
18. J. Yang, M. Kuwabara, T. Asano, A. Chuma, and J. Du: *ISIJ Int.*, 2007, vol. 47 (10), pp. 1401–08.
19. K. Takahashi, K. Utagawa, H. Shibata, and S.K. Naoki: *ISIJ Int.*, 2012, vol. 52 (1), pp. 10–17.
20. W.T. Lou and M.Y. Zhu: *Metall. Mater. Trans. B*, 2014, vol. 45B, pp. 1706–22.
21. W.T. Lou and M.Y. Zhu: *ISIJ Int.*, 2015, vol. 55 (5), pp. 961–69.
22. C.J.W. Fincham and F.D. Richardson: *J. Iron Steel Inst.*, 1954, vol. 178, pp. 4–15.

23. M. Hino, S. Kitagawa, and S. Ban-ya: *ISIJ Int*., 1993, vol. 33 (1), pp. 36–42.
24. T. Fujisawa, S. Inoue, S. Takagi, Y. Wanibe, and H. Sakao: *Tetsu-to-Hagané*, 1985, vol. 71 (7), pp. 839–45.
25. B.Y. Shiro, H. Makoto, K. Tetsuro, and M. Hino: *ISIJ Int*., 2004, vol. 44 (11), pp. 1810–16.
26. J.X. Cheng: *The Common Use Handbook of Diagram for Steelmaking*, Metallurgical Industry Press, Beijing, 2010, p. 818.
27. Y. Ozawa and K. Mori: Trans*Iron Steel Inst. Jpn*., 1983, vol. 23 (9), pp. 764–68.
28. L.R. Farias and G.A. Irons: *Metall. Mater. Trans. B*, 1985, vol. 16B, pp. 211–25.
29. T.A. Engh and A Johnston: *Proc. Int. Symp. on Reduction and Casting of Aluminum*, Pergamon, New York, NY, 1988, pp. 11–20.
30. D.E. Langberg, S. Avery, and M. Nilmani: *Metall. Mater. Trans. B*, 1996, vol. 27B, pp. 773–79.
31. D. Liu, Q. He, and G.M. Evans: *Adv. Powder Technol*., 2010, vol. 21 (4), pp. 401–11.
32. W.T. Lou and M.Y. Zhu: *Metall. Mater. Trans. B*, 2013, vol. 44B, pp. 1251–63.
33. A.R. Sarhan, J. Naser, and G. Brooks: *Int. J. Miner. Process*., 2016, vol. 146, pp. 54–64.
34. A.R. Sarhan, J. Naser, and G. Brooks: *Can. Metall. Q*., 2017, vol. 56, pp. 45–57.
35. M.A. Sattar, J. Naser, and G. Brooks: *Chem. Eng. Sci*., 2014, vol. 107, pp. 165–80.
36. M.A. Sattar, J. Naser, and G. Brooks: *Chem. Eng. Sci*., 2013, vol. 94, pp. 69–78.
37. P.H. Calderbank and M. Moo-Young: *Chem. Eng. Sci*., 1961, vol. 16 (1–2), pp. 39–54.
38. P. Harriott: *AIChE J*., 1962, vol. 8 (1), pp. 93–102.
39. P.L.T. Brian, H.B. Hales, and T.K. Sherwood: *AIChE J*., 1969, vol. 15 (5), pp. 727–33.
40. D.M. Levins and J.R. Glastonbury: *Chem. Eng. Sci*., 1972, vol. 27 (3), pp. 537–42.
41. J. Garside and S.J. Jancic: *AIChE J*., 1976, vol. 22 (5), pp. 887–94.
42. M.A. Piero and J.K. Donald: *Chem. Eng. Sci*., 1989, vol. 44 (12), pp. 2781–96.
43. J.C. Lamont and D.S. Scott: *AIChE J*., 1970, vol. 16 (4), pp. 513–19.
44. Z.F. Cheng and M.Y. Zhu: *Materials Processing Fundamentals,* TMS 2013 Annual Meeting, San Antonio, TX, 2013, TMS, Warrendale, PA, pp. 291–303.
45. K. Krishnapisharody and G.A. Irons: *Metall. Mater. Trans. B*, 2006, vol. 37B, pp. 763–72.
46. K. Krishnapisharody and G.A. Irons: *ISIJ. Int*., 2008, vol. 48, pp. 1807–09.